Ni$_{0.6-x}$Mo$_{0.4-x}$Ir$_x$-oxide as an electrode material for supercapacitors: investigation of the influence of iridium content on the charge storage/delivery

Abraham Gomez Vidales[1] · Jaewoo Kim[1] · Sasha Omanovic[1]

Abstract

Ni$_{0.6-x}$Mo$_{0.4-x}$Ir$_x$-oxide coatings were fabricated with the purpose of investigating the influence of Ir content on their charge storage/delivery capability when used as an electrode for electrochemical supercapacitor. Experimental work in alkaline medium confirmed that the amount of Ir in the Ni-Mo-oxide significantly influences the material's charge storage capacity. The highest overall capacitance (108 ± 2 mFcm^{-2} at 1 mA cm^{-2}) was obtained for the composition containing 40 mol% of Ir (Ni$_{0.36}$Mo$_{0.24}$Ir$_{0.4}$-oxide), while the best candidates in terms of the intrinsic (surface area–independent) charge storage/delivery are the compositions containing 20 and 40 mol% of Ir (no statistical difference). Ni$_{0.36}$Mo$_{0.24}$Ir$_{0.4}$-oxide was found to retain ca. 86% of its initial capacitance after 2500 charge-discharge cycles, at 1 mA cm^{-2}.

Introduction

Efficient, affordable, sustainable, and clean sources of energy production and storage are required to address the current energy crisis and global warming [1]. Electrochemical supercapacitors (ES) are promising energy storage devices that have garnered much interest due to their high power density, fast charge-discharge rate, and long-life cycling capability [2, 3]. In addition, they can complement or even replace batteries in some instances, especially when high power delivery is needed [4]. ES have attracted much attention due to their application in portable electric devices and electric vehicles. In recent years, extensive work has focused on ways to increase their specific energy density and lower their production costs.

ES are classified into two types based on their charge storage mechanisms: electrical double-layer capacitors (EDLCs) based on the double-layer capacitance where electrostatic forces store energy at the electrode/electrolyte interface, and pseudocapacitors, also known as faradaic supercapacitors, which are based on the pseudocapacitance arising from fast reversible faradaic reactions occurring at the (sub) electrode

surface [5]. In general, both energy storage mechanisms, electrostatic and faradaic, coexist in a supercapacitor, although it is always one of the two that determines their overall behavior.

For ES, the capacitance relies heavily upon the electrode materials used. Three types of electrode materials are usually employed in ES: carbon materials, conducting polymers, and metal oxides [6, 7]. Carbon-based materials, used mainly in EDLCs, exhibit a low charge storage capacity, which in turn limits their practical applications in certain cases. On the other hand, conducting polymers and metal oxides, commonly used as electrode materials for pseudocapacitors, yield a significantly higher specific capacitance when compared with EDLCs [8–10]. Specifically, transition metal oxides (TMOs) have been recognized as the most promising electrode materials to be used in ES [11, 12] due to their relatively good conductivity, large specific capacitance, and much longer life cycles in comparison with conducting polymers [11, 13–16]. TMOs such as ruthenium, iridium, manganese, nickel, and molybdenum oxides can provide high energy density and a superior capacitance due to the several oxidation states which facilitate redox reactions [2, 17, 18].

Iridium oxide was found to be a promising material as an electrochemical supercapacitor electrode due to its high specific capacitance, high conductivity, and excellent electrochemical reversibility [2, 4, 19]. Even with its unique properties as an electrode for ES applications, its high cost has restricted its extensive utilization. Therefore, alternative electrode materials, such as nickel and molybdenum oxides,

✉ Abraham Gomez Vidales
abraham.gomezvidales@mail.mcgill.ca

1 Department of Chemical Engineering, McGill University, 3610 University St., Montreal, Quebec H3A 0C5, Canada

which are inexpensive and exhibit excellent pseudocapacitive behavior, have been explored [7]. Specifically, nickel oxide has been employed recently in rechargeable batteries and electrochemical supercapacitors, owing to its low cost and availability [5, 20, 21]. Furthermore, it is known that the combination of nickel oxides with other oxides not only reduces the cost but also improves the electrode stability [22–24] and could enhance the power capability due to its amorphous nature and porous structure, which significantly improves the charge transfer and capacitance of an electrode [20, 25].

Taking into account, on one side, that Ir-oxide offers high specific capacitance but is a rather expensive material and, on the other side, that Ni-based oxide materials also offer relatively high specific capacitance values, but are significantly cheaper; in this research study, we report results of the investigation of combining air- and a Ni-Mo-based oxide to produce a high capacitance and cost-effective electrode material for supercapacitors. More specifically, the influence of Ir-oxide content on the charge storage/delivery capability of $Ni_{0.6-x}Mo_{0.4-x}Ir_x$-oxide electrodes was investigated. It should be noted that the aim of this study was only to screen (compare) potential electrode combinations for their charge storage/delivery, rather than designing a nanostructured combination of the same and their three-dimensional structure optimization for testing in a two-electrode (electrochemical supercapacitor) cell, which is the next step of our project.

Experimental

Material synthesis

Ni-Mo-Ir-oxide coatings were prepared by dissolving $NiCl_2 \times 6H_2O$ (purity 99.9%, Sigma-Aldrich, Canada), $Na_2MoO_4 \times 2H_2O$ (purity 99.5 wt%; Sigma-Aldrich, Canada), and $IrCl_3 \times 3H_2O$ (purity 99.9 wt%; Sigma-Aldrich, Canada) in an equivolume mixture of HCl (37 wt%; Fisher Scientific, Canada) and nanopure water (resistivity 18.2 MΩ cm). Ni and Mo were always mixed in a 60:40 M ratio, while the percentage of Ir was varied from 0 to 100 mol% (relative to the Ni/Mo amount). Titanium buttons (1.27-cm diameter, 0.2-cm thickness, purity 99.2%, Alfa Aesar, USA) were used as a substrate. First, the Ti buttons were polished with 600 grit polishing paper (Anamet, Canada). The Ti substrates were then sonicated in deionized water for 10 min to remove any residue. Next, they were etched in a mixture of HCl and nanopore water (1:1 by volume) for 30 min and dried with argon gas (MEGS Specialty Gases Inc., 99.998 wt% pure, Canada). The coating solution was applied uniformly on one side of the prepared substrate using a standard paintbrush. The substrates were placed in an oven at 373 K for 5 min to vaporize the solvent and then annealed for 15 min at 773 K in a furnace. The samples were then cooled to ambient temperature for 10 min. The procedure was repeated until six coatings were applied. For the last coating, the plate was annealed in the furnace for 1 h (at 773 K) to oxidize the metal coating. Finally, the resulting electrode was sonicated for 10 min in a nanopure water bath and dried with argon.

Material characterization

Scanning electron microscope (SEM) was used to investigate the surface morphology and structure of the samples. Energy-dispersive spectroscopy (EDS) was conducted to quantify the content of the elements in the coating. Both measurements were performed on a Hitachi SU-3500 Variable Pressure SEM (Hitachi, Japan) microscope with EDS detector. X-ray photoelectron spectroscopy (XPS) was used to examine the surface chemical composition of the coatings employing the Thermo Scientific K-Alpha X-ray photoelectron spectrometer (Thermo Fisher Scientific, USA). A goniometer model OCA 15EC equipped with a CCD camera (Data Physics, USA) was used to measure the contact angle. Finally, the surface roughness and coating thickness were measured using a DektakXT stylus (Bruker, USA) surface profilometer.
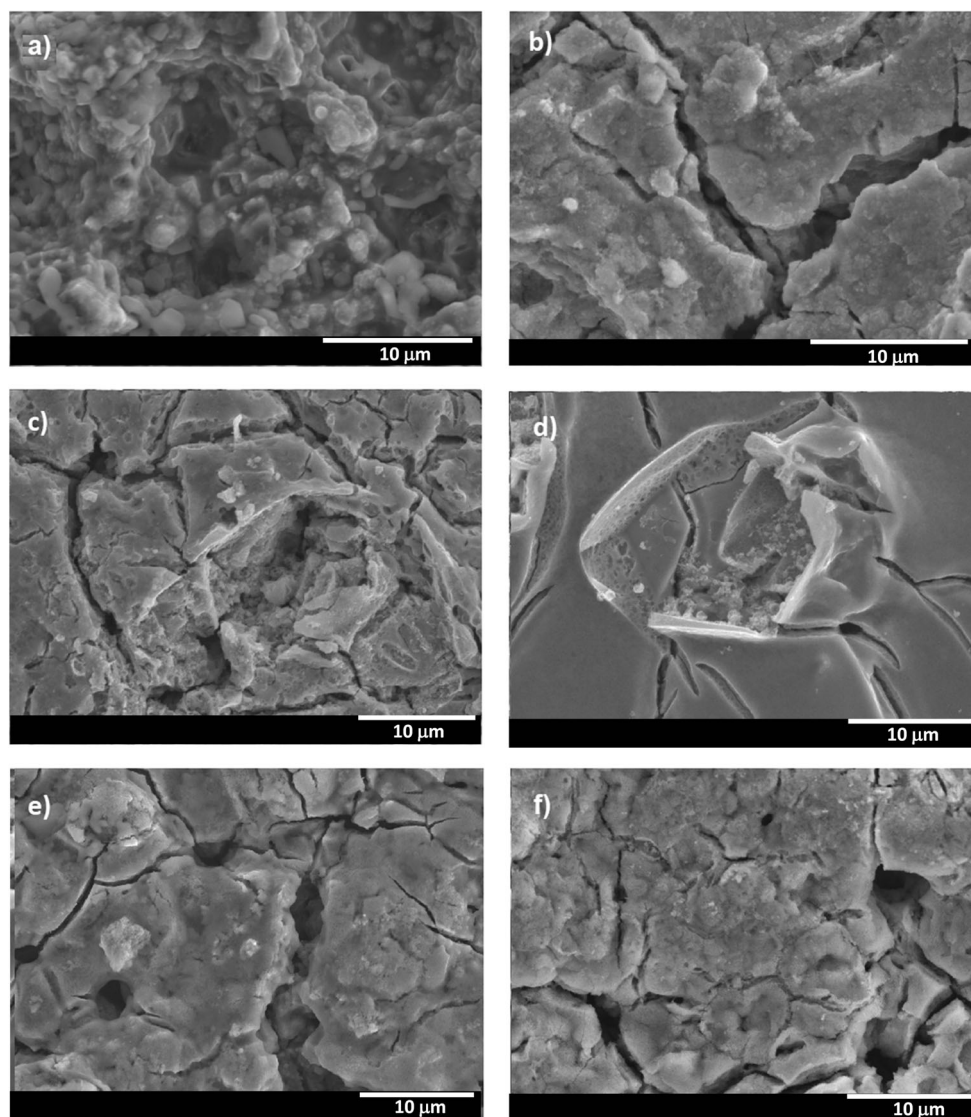
Electrochemical characterization

The electrochemical behavior of electrodes was characterized using cyclic voltammetry (CV) and galvanostatic charge-discharge (GCD) cycling to evaluate their performance and potential suitability as supercapacitor electrodes. A two-electrode coin-type cell was employed. The cell configuration included two Ni-Mo-Ir-oxide working electrodes (WEs) with the coated side facing each other, separated by a filter paper (P5 Grade, Fisher Scientific, USA) immersed in aqueous 6-M KOH electrolyte. Furthermore, a three-electrode system was also employed, to investigate the electrochemical behavior of the best-performing electrode ($Ni_{0.36}Mo_{0.24}Ir_{0.4}$-oxide). In this setup, this electrode was used as a working electrode, a graphite rod was employed as a counter electrode, and a standard calomel electrode (SCE) (Accumet electrode, Fisher Scientific, USA) served as a reference electrode. The geometric area of the electrode exposed to the electrolyte solution was 1.27 cm^2. All electrochemical measurements were performed using a potentiostat/galvanostat analyzer (Autolab PGSTAT30, Metrohm, The Netherlands) controlled by the NOVA software (v. 2.1.3; Metrohm, The Netherlands).

Results and discussion

Physical characterization of the Ni-Mo-Ir-oxides

Figure 1 depicts the morphology of the Ni-Mo-Ir-oxide coatings. The prepared coatings have a uniform morphological

Fig. 1 SEM images of $Ni_{0.6}Mo_{0.4}$-oxide (**a**), $Ni_{0.48}Mo_{0.32}Ir_{0.2}$-oxide (**b**), $Ni_{0.36}Mo_{0.24}Ir_{0.4}$-oxide (**c**), $Ni_{0.24}Mo_{0.16}Ir_{0.6}$-oxide (**d**), $Ni_{0.12}Mo_{0.08}Ir_{0.8}$-oxide (**e**), and Ir-oxide (**f**) coatings. The overall scale length on the images is 10 μm

distribution with an average thickness of 5 ± 2 μm (determined in separate measurements). It is noted that the addition of Ir to the Ni-Mo-oxide changes the surface morphology of the coatings. The coating without Ir (Fig. 1a) has a porous granular-type structure. Meanwhile, the coatings that contain Ir (Fig. 1b–f) have a cracked-mud/cauliflower-like morphology. This cracked-mud structure provides easy mobility for the ions to access the electrode/electrolyte interface, which is a crucial factor for the surface redox reactions. According to the literature, these surface morphologies are commonly observed in the Ir-oxide and Ni-oxide surfaces produced by thermal decomposition [26, 27].

The microscale surface roughness, *Ra*, was determined using a stylus profilometer, while the electrochemically active surface area (EASA) was obtained based on the double-layer capacitance (for more detail about how the EASA was calculated, please refer to our previous publication [24]). As shown in Table 1, both sets of values follow a similar tendency,

indicating that the microscale surface roughness directly extrapolates to the nanoscale surface porosity. The addition of Ir into the base metal oxide coating ($Ni_{0.6}Mo_{0.4}$-oxide) resulted in both an increase in the surface roughness and active surface area of the electrode, which should have a positive impact on the capacitance.

Table 1 Surface roughness and electrochemically active surface area of Ni-Mo-oxide and Ni-Mo-Ir-oxide coatings

Sample	Roughness Ra (μm)	EASA (cm^2)
$Ni_{0.6}Mo_{0.4}Ox$	0.46 ± 0.02	21.0 ± 3.5
$Ni_{0.48}Mo_{0.32}Ir_{0.2}Ox$	0.64 ± 0.07	29.3 ± 1.5
$Ni_{0.36}Mo_{0.24}Ir_{0.4}Ox$	1.25 ± 0.11	32.4 ± 2.5
$Ni_{0.24}Mo_{0.16}Ir_{0.6}Ox$	1.29 ± 0.13	44.8 ± 8.0
$Ni_{0.12}Mo_{0.08}Ir_{0.8}Ox$	1.42 ± 0.09	72.5 ± 6.0
IrOx	1.93 ± 0.10	86.5 ± 20.0

Electron-dispersive spectroscopy (EDS) was used to esti-mate the elemental composition of the Ni-Mo-Ir-oxide coat-ings. In all the coatings, peak characteristics of Ni, Mo, and Ir were obtained. This proves the presence of these metals on the electrode surface.

Table 2 shows the normalized results. The nominal values are very similar to the resulted EDS-determined values. This confirms that the desired composition of coatings is achieved through the thermal-salt decomposition method. Moreover, since the measurements were done in three different sections of the coating, this also proves that the elements were homo-geneously distributed.

To confirm the top-surface composition of the oxide coat-ings produced, X-ray photoelectron spectroscopy (XPS) mea-surements were carried out on selected compositions. The surface of each sample was examined at three different loca-tions to ensure the reliability of the results. The binding energy scale was referenced to the C 1s signal at 284.5 eV. Typical survey spectra for ternary oxide revealed that all electrode composition elements are present at the surface with the Ni, Mo, and Ir photoelectron peaks found at 885–845, 235–225, and 70–55 eV, respectively. Table 3 shows the relative atomic percentage of the elements present on the topmost surface of the coatings. The relative composition of this topmost surface layer agrees well with the nominal (bulk composition) and also with previous results obtained by EDS (Table 2).

After the general scan was made, high-resolution binding energy spectra for Ni 2p, Mo 3d, Ir 4f, and O 1s regions were recorded for the $Ni_{0.36}Mo_{0.24}Ir_{0.4}$-oxide coating (the sample that yielded the highest capacitance, as shown later in the text), and the results are presented in Fig. 2. Figure 2a shows the Ni 2p spectrum; the Ni $2p_{3/2}$ photoelectron peak is visible at 854.3 eV and two satellite peaks at 859.8 and at 864.3 eV. Besides, Ni $2p_{1/2}$ photoelectron peak at 871.7 and a satellite peak at 878.3 eV are also visible on the spectrum. The spec-trum confirms the presence of NiO, Ni_2O_3, and nickel halides ($NiCl_2$) on the coating surface. Figure 2b presents the Mo spectrum with peaks for 3 $d_{5/2}$ and 3 $d_{3/2}$, which suggests the presence of Mo, MoO_2, and MoO_3, which characteristic peaks at 228.2, 229.7, and 231.5 eV, respectively.

Table 2 Relative atomic percentage of Ni, Mo, and Ir in the oxide coatings (excluding the contribution of oxygen and other impurities in the coatings) obtained by EDS

Nominal	Results
$Ni_{0.6}Mo_{0.4}Ox$	$Ni_{0.63}Mo_{0.37}Ox$
$Ni_{0.48}Mo_{0.32}Ir_{0.2}Ox$	$Ni_{0.50}Mo_{0.26}Ir_{0.24}Ox$
$Ni_{0.36}Mo_{0.24}Ir_{0.4}Ox$	$Ni_{0.45}Mo_{0.20}Ir_{0.35}Ox$
$Ni_{0.24}Mo_{0.16}Ir_{0.6}Ox$	$Ni_{0.38}Mo_{0.13}Ir_{0.51}Ox$
$Ni_{0.12}Mo_{0.08}Ir_{0.8}Ox$	$Ni_{0.18}Mo_{0.10}Ir_{0.72}Ox$
IrOx	IrOx

Table 3 Relative atomic percentage of Ni, Mo, and Ir in the oxide coatings (excluding the contribution of oxygen and other impurities in the coatings) obtained by XPS in selected electrodes

Nominal	Results
$Ni_{0.6}Mo_{0.4}Ox$	$Ni_{0.58}Mo_{0.42}Ox$
$Ni_{0.48}Mo_{0.32}Ir_{0.2}Ox$	$Ni_{0.47}Mo_{0.25}Ir_{0.28}Ox$
$Ni_{0.36}Mo_{0.24}Ir_{0.4}Ox$	$Ni_{0.34}Mo_{0.20}Ir_{0.46}Ox$
IrOx	IrOx

Additionally, the spectrum evidences that MoO_3 is the pre-dominant form of Mo-oxide on the outer part of the coating surface.
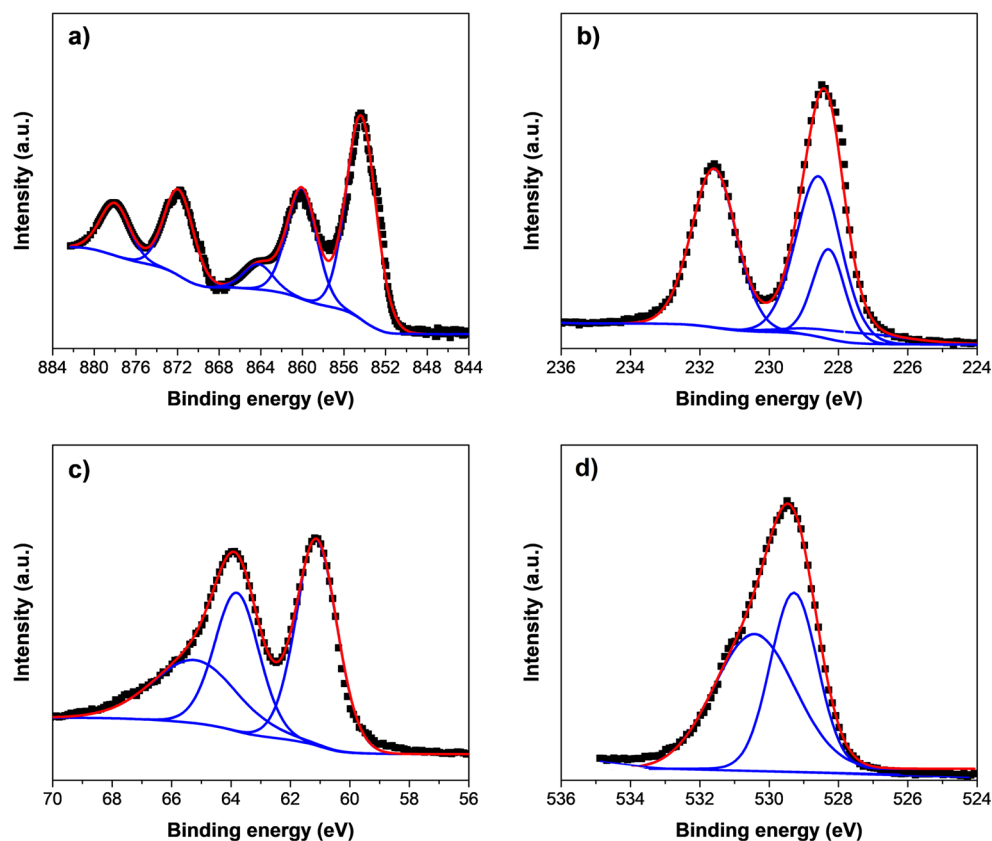
Figure 2c displays the spectrum for the Ir 4f region. The peaks located at binding energy values of 60.8, 63.7, and 65.6 eV correspond to Ir $4f_{7/2}$ and Ir $4f_{5/2}$ levels of Ir^{4+}. These peaks confirm the presence of iridium in the metallic, $IrCl_3$, and IrO_2 forms [28]. Finally, in Fig. 2d, the O 1s spec-trum is shown. The high-resolution binding energy spectrum can be deconvoluted into two types of components. The deconvoluted peak at 529.3 eV represents oxygen in a crystal lattice (O^{2-}), while the peak at 530.7 eV represents oxygen in the hydroxyl group (OH^-) [29]. Hence, the Ni-Mo-Ir-coating compounds are metal oxides and metal hydroxides existing in an approximate ratio of 1.5:1. As a result, it can be assumed that the capacitance not only depends on the oxides but is also increased by the presence of metal hydroxides [30].

To study the interaction at the electrode/electrolyte inter-face (wettability), contact angle measurements were carried out based on the sessile drop method. Table 4 displays the average of contact angles of the Ni-Mo-Ir-oxide coatings. As can be seen from the table, they exhibit an intrinsically hydro-philic behavior, as the water contact angle is between 22° ± 0.6 and 29° ± 2.1 indicating high wettability. This may result due to the strong cohesive force between the water droplet and hydroxide present in the oxide compounds and also due to the porous nature of the coatings, which favors the easy interca-lation of the H^+ ions in the electrolyte, favoring ionic conduc-tivity and subsequently increasing the capacitance [31]. However, the data show that there is not a clear relation be-tween the Ir content and the wettability.
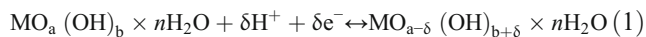
Electrochemical performance of the Ni-Mo-Ir-oxides as supercapacitors

Cyclic voltammetry (CV) was first employed to evaluate the capacitive behavior of the Ni-Mo-Ir-oxides as supercapacitors in the alkaline medium in a two-electrode cell. As an example, CVs of the $Ni_{0.36}Mo_{0.24}Ir_{0.4}$-oxide electrode recorded at sev-eral scan rates are displayed in Fig. 3a. The voltammograms exhibit a semi-rectangular shape characteristic of electrochem-ical supercapacitors. Although metal oxides were used, no

Fig. 2 Ni 2p XPS spectrum (**a**), Mo 3d XPS spectrum (**b**), Ir 4f XPS spectrum (**c**), and O1s XPS spectrum (**e**) of the $Ni_{0.36}$ $Mo_{0.24}Ir_{0.4}$-oxide coating. The black points represent experimental data, the red line represents the corresponding simulated spectrum, and the blue lines represent deconvoluted contributions of the major peaks

redox peaks were recorded. Only at the highest scan rate, a very broad anodic and cathodic "shoulder" can be seen, indicating the presence of several overlapping redox peaks. It should be noted that the charge under the CV is related to both the electrostatic charging of the double-layer and reversible redox reactions in the solid phase. As it will be shown in the following sections, the contribution of the latter is significantly higher. The reversible solid-phase reactions can be related to reversible transitions of the three metals to different oxidative states, which could be, in a general way, presented as:

$$MO_a(OH)_b \times nH_2O + \delta H^+ + \delta e^- \leftrightarrow MO_{a-\delta}(OH)_{b+\delta} \times nH_2O \quad (1)$$

where it is seen that intercalation of H^+ in the solid phase is required in order to balance the charge.

Table 4 Average contact angles measured immediately after the droplet touched the surface

Sample	Contact angle (°)
$Ni_{0.6}Mo_{0.4}Ox$	29 ± 2.1
$Ni_{0.48}Mo_{0.32}Ir_{0.2}Ox$	23 ± 1.4
$Ni_{0.36}Mo_{0.24}Ir_{0.4}Ox$	25 ± 1.7
$Ni_{0.24}Mo_{0.16}Ir_{0.6}Ox$	22 ± 0.6
$Ni_{0.12}Mo_{0.08}Ir_{0.8}Ox$	26 ± 1.5
$IrOx$	24 ± 0.9

To calculate the capacitance of the metal oxide electrodes produced, from CV measurements, Eq. 2 can be used [4]:

$$C = \frac{\int IdV}{2A\Delta ES} \quad (2)$$

where C is the capacitance (mF cm^{-2}), $\int IdV$ is the integrated anodic or cathodic area enclosed in the CV curve (mA s), A is the geometric area of the electrode exposed to the electrolyte (cm^{-2}), ΔE is the scanned potential range (V), and S is the scan rate (V s^{-1}). Figure 3b shows the corresponding variation of capacitance of the Ni-Mo-Ir-oxide electrodes investigated in this work as a function of scan rate. The observed capacitance values of some Ni-Mo-Ir-oxide compositions are higher than the values reported for some oxides such as NiO [32] (74.8 mF cm^{-2} at a scan rate of 10 mV s^{-1}).

The decrease in capacitance with the scan rate is commonly observed in the literature [2, 16, 33, 34]. This is to expect since at higher scan rates, the redox zone in the solid phase is "shallower," i.e., there is not sufficient time for the electrolyte ions (H^+) to diffuse (intercalate) deeper under the oxide surface and compensate the metal redox charge change (Eq. 1); i.e., only the outer active surface is utilized for charge storage [10, 15, 21]. Similar behavior is reported in the literature for various electrode materials [2, 8]. In the case of an IrO_2 supercapacitor, this effect is attributed to the increment of
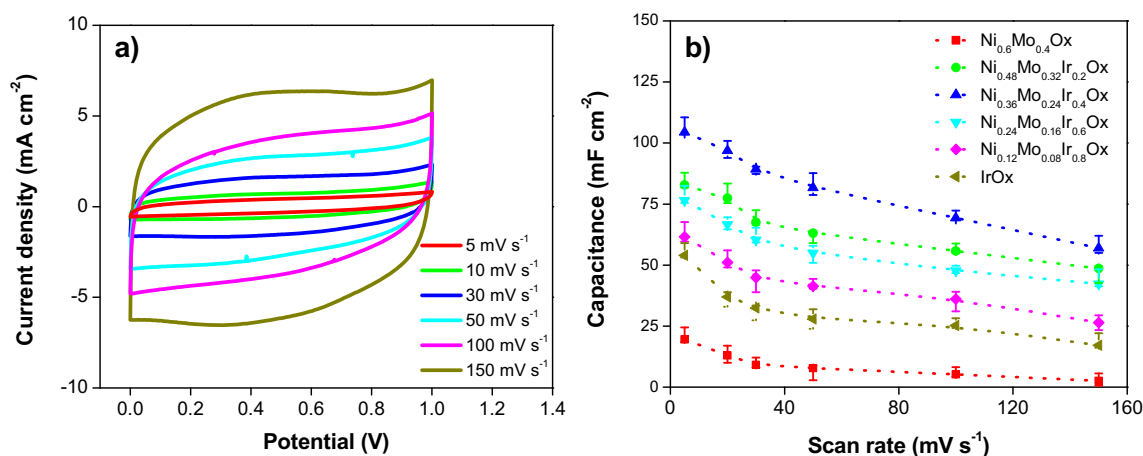
Fig. 3 **a** Cyclic voltammograms of the $Ni_{0.36}Mo_{0.24}Ir_{0.4}$-oxide electrode recorded in 6 M KOH. **b** Variation of capacitance with scan rates calculated from CVs recorded on different Ni-Mo-Ir-oxide electrodes in 6 M KOH

the ionic resistance inside the pores and the weak electric contact between the electrolyte/electrode [35, 36].

The lowest capacitance values were obtained with the $Ni_{0.6}$-$Mo_{0.4}$-oxide coating (no Ir content), while the next higher capacitance was obtained for pure Ir-oxide. All Ni-Mo-Ir-containing oxide compositions yielded higher capacitance values. When Ir is added (20 wt%) to the Ni-Mo-oxide coating, the capacitances increased around three times with respect to $Ni_{0.6}$-$Mo_{0.4}$-oxide. The highest capacitances were obtained when the Ir content reached 40 wt%. After this Ir content, the capacitances decreased gradually. This provides evidence that the behavior of the oxide coatings is significantly dependent on the coating composition and is not a linear function of Ir content.

Previous studies on Ir and Ir-oxide attributed the increase of the capacitance to the growth of the electrochemically active surface area [13]. As shown in Table 1, with the increase of Ir content, the electrochemically active surface area (EASA) of the coatings increases linearly ($R^2 = 0.961$). Nevertheless, this linear trend could (potentially) explain the increase in capacitance from 0 to 40% of Ir in the coating, but not the decrease in capacitance after this composition; even the pure Ir-oxide sample (which has the largest EASA) has lower capacitance values compared with all the Ni-Mo-Ir-oxide coatings. This proves that the addition of Ir to the Ni-Mo-oxide coatings improved the pseudocapacitive properties compared with pure Ir-oxide and the existence of a maximum (at 40% of Ir in the coating) also indicates that probably the combination of these three metal oxides produced a maximum synergistic effect on this composition. Therefore, the improved capacitance of the Ni-Mo-Ir-oxide coatings could be due to the activation of non-stoichiometric sites of the precursor's species in the oxide films, the increment of the electrical conductivity of the electrodes and ion diffusion (intercalation) rate, and not only to the enhancement of the electrochemically active surface area [2, 8, 37].

To further investigate the performance and cycle life of the Ni-Mo-Ir-oxide coatings, galvanostatic charge-discharge

(GCD) experiments were performed [19]. GCD measurements were conducted at different current densities (1, 3, 5, and 10 mA cm^{-2}) for 250 cycles in a 6-M KOH solution in a two-electrode cell. As a representative example, Fig. 4a shows the GCD curves for the 250th cycle of the $Ni_{0.36}Mo_{0.24}Ir_{0.4}$-oxide electrode at different charge-discharge current densities. All the electrodes displayed the triangular charge-discharge behavior traditionally observed in electrochemical supercapacitors. The slight deviation from linearity suggests a pseudocapacitive behavior which is the result of the electrochemical redox reactions occurring in the solid phase within the electrode sub-surface (Eq. 1) and is in accordance with CV measurements presented previously in the text [20]. As expected, with an increase in charge-discharge current, the GCD curves move to shorter times.

GCD curves were used to calculate the capacitance of the electrodes employing Eq. 3:

$$C = \frac{\int I dt}{\Delta E A} \qquad (3)$$

where C is the capacitance (mF cm^{-2}), I is the current applied for the charge-discharge (mA), t is the time elapsed for the charge-discharge cycle (s), A is the geometric area of the electrode exposed to the electrolyte (cm^{-2}), and ΔE is the corresponding potential interval of the charge-discharge cycle (V) [38].

Figure 4b shows the capacitance of the Ni-Mo-Ir-oxide electrodes as a function of current density. The capacitance was determined by averaging the values recorded in the last 50 cycles after the capacitance was stabilized. As it was expected, the capacitance values followed the same trend as the ones obtained from CV and could be explained in the same manner. Again, the maximum capacitance was reached when the content of Ir was 40%. Research by Ullah et al. [39] examined the capacitance of several compositions of Ir_xRu_{1-x}-
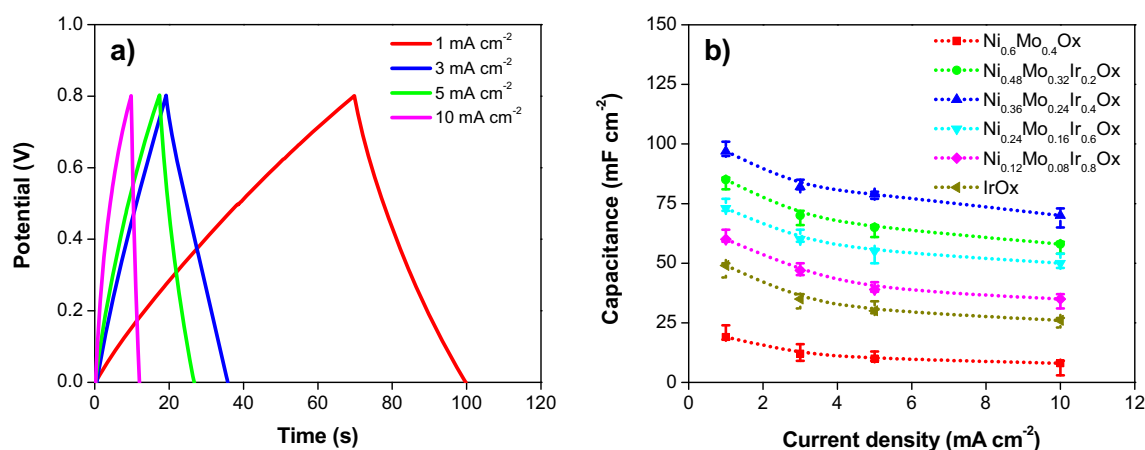
Fig. 4 **a** The 250th full charge-discharge cycle of $Ni_{0.36}Mo_{0.24}Ir_{0.4}$-oxide electrode recorded in 6-M KOH at various current densities. **b** Capacitance as a function of charge-discharge current density of different Ni-Mo-Ir-oxide electrodes obtained from GCD curves recorded in 6 M KOH

oxide coatings, and they also found a considerable increase (sixfold in their case) in capacitance when the Ir content reached 40% in this particular metal oxide. However, they obtained a lower capacitance, ca. 85 mF cm^{-2}, with $Ir_{0.4}$-$Ru_{0.6}$-oxide and also at a significantly lower current density, 0.1 mA cm^{-2}. Similar studies using metal oxides obtained lower capacitances values, i.e., ZnO/MnO_2 [40] (14 mF cm^{-2} at a current density of 0.1 mA cm^{-2}) and pure Ru-oxide [39] (35–39 mF cm^{-2} at a current density of 0.1 mA cm^{-2}). This demonstrates that the $Ni_{0.36}Mo_{0.24}Ir_{0.4}$-oxide electrode is an excellent candidate for supercapacitors.

In all the cases, a gradual decrease in capacitance occurred when the current density was increased (Fig. 4b). This behavior is commonly reported in the literature on supercapacitor electrodes [38, 39, 41, 42] and, in the current case, it can be related to a decrease in the depth zone of oxide utilization. Namely, with an increase in charge-discharge current density, the corresponding overpotential also increases (this overpotential is related to both the electron-transfer and ion-transport rate, Eq. 1). Consequently, the charging potential limit is reached at shorter times (Fig. 5), minimizing the depth of penetration of protons deeper into the metal oxide structure. This, in turn, results in a decrease in charge (i.e., capacitance) storage/delivery, as a shallower metal oxide zone is used.

An electrochemical impedance spectroscopy spectrum of the best-performing $Ni_{0.36}Mo_{0.24}Ir_{0.4}$-oxide was recorded at 0 V, and the result is presented in the form of a Nyquist plot in Fig. 5. The shape of the spectrum reveals a pseudocapacitive behavior. Namely, three-time constants can be observed: two well-profiled capacitive semicircles in the mid (main plot) and high-frequency region (inset) and a semi-linear behavior in the low-frequency region. The time constant at high frequencies (τ_1) can be related to the electrostatic double-layer charging, while the one at mid frequencies (τ_2) represents the response of the pseudocapacitive charging (Eq. 1). The semi-linear response at low frequencies (τ_3) can be related to slow mass-

transport of protons in the oxide phase (Eq. 1). The intersection of the spectrum with the real impedance axis at high frequencies represents the equivalent series resistance, and the corresponding value is 5.7 Ω cm^2.

As mentioned earlier, the capacitance values presented in Figs. 3b, 4b are the results of both the electrostatic double-layer charging and redox reactions in the solid phase (Eq. 1). While both depend on the surface area of the electrode exposed to the electrolyte, the latter also depends on intrinsic properties of the oxide phase (crystalline structure and distribution of oxides). In order to estimate the influence of Ir content in the oxide on the redox-related capacitance only, GCD capacitance values recorded at 1 mA cm^{-2} were normalized with respect to the electrochemically active surface area. The corresponding trend is presented in Fig. 6. As seen, the highest contribution to the redox charge storage (pseudocapacitance) is offered by electrodes containing 20% and 40% of Ir (there is
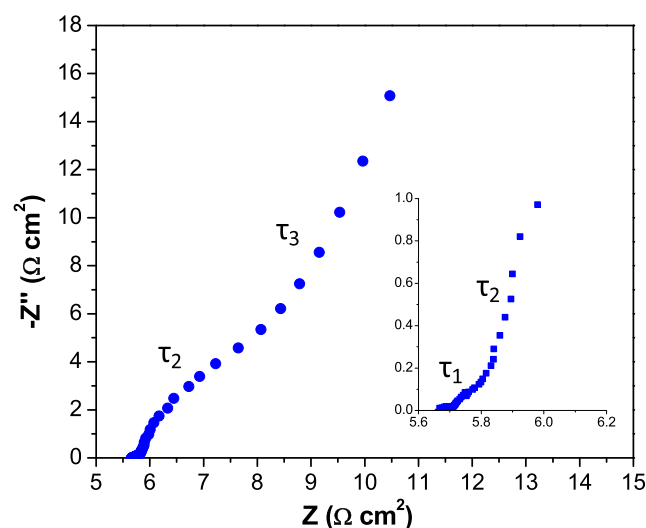

Fig. 5 Nyquist plot of the $Ni_{0.36}Mo_{0.24}Ir_{0.4}$-oxide electrode. The inset shows an expanded view of the mid and high-frequency regions
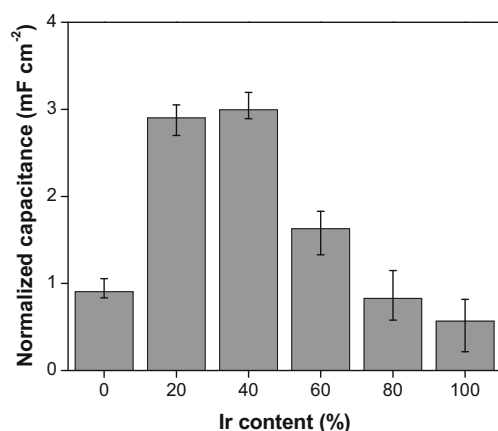
Fig. 6 GCD intrinsic capacitance values (normalized with respect to the electrochemically active surface area) recorded at 1 mA cm^{-2} as a function of Ir content

no statistical difference between the two capacitance values offered by these two compositions). Thus, these compositions are intrinsically the best among the investigated ones for pseudocapacitive charge storage/delivery. As already mentioned before, the improved capacitance of the Ni-Mo-oxide that contains Ir could be due to the activation of non-stoichiometric sites of the precursor's species in the oxide films, the increment of the electrical conductivity of the electrodes and ion diffusion (intercalation) rate [2, 8, 37].

Figure 7 shows the Ragone plot of the Ni-Mo-Ir-oxide electrodes studied in this work obtained from GCD measurements (discharge cycle). As shown, all the Ni-Mo-Ir-oxide coatings studied here offer better performance than pure Ir-oxide, with Ni$_{0.36}$-Mo$_{0.24}$-Ir$_{0.4}$-oxide offering the best performance. This sample delivers an energy density of ca. 64 mWh m^{-2} at a power density of 23 W m^{-2}. These results are promising, considering the low amount of iridium incorporated into the oxide.

In order to characterize the best-performing electrode material (Ni$_{0.36}$-Mo$_{0.24}$-Ir$_{0.4}$-oxide) in more detail, cyclic voltammetry measurements were performed in a three-
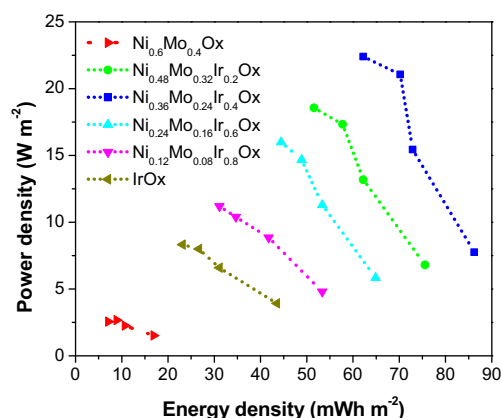
electrode electrochemical cell. Figure 8 shows a cyclic voltammogram of the Ni$_{0.36}$-Mo$_{0.24}$-Ir$_{0.4}$-oxide electrode recorded in a wide potential window. At potentials negative of ca. −1.3 V, hydrogen evolution occurs. From ca. −1.3 to 0 V, a capacitive region is displayed in the anodic scan, followed by a broad current peak at ca. 0.4 V, probably composed of several overlapping peaks. This broad current peak can be related to the oxidation of the three metals comprising the oxide into their higher oxidation state [43–45]. The further increase in potential results in oxygen evolution, commencing at ca. 0.6 V. In the returning scan, the metal oxides formed in the anodic scan are reduced to their initial state, as indicated by the appearance of a cathodic peak at ca. 0 V and a broad "shoulder" (representing overlapping peaks) in the potential region between 0 and −1.3 V.

Further characterization of the electrochemical behavior of Ni$_{0.36}$-Mo$_{0.24}$-Ir$_{0.4}$-oxide was done by recording cyclic voltammograms at various scan rates, in the potential region between hydrogen evolution and anodic oxidation peak, which represents the capacitive region in Fig. 8, and the results are presented in Fig. 9a. With an increase in scan rate, the current also increases. In order to determine whether this increase in the current is controlled by mass-transport or it is related to surface processes, the dependence of anodic and cathodic current at −0.6 V is analyzed with respect to scan rate [46]. A plot of current vs. scan rate resulted in a curved line (not shown here), indicating that the response is not controlled by surface reactions (e.g., adsorption or electrostatic double-layer charging). On the other hand, the dependence of current on the square root of scan rate was linear, as seen in Fig. 9b, indicating that the electrochemical response around the investigated potential is controlled by mass transport. Taking into account that the pseudocapacitive charge-discharge of the oxide electrodes studied here proceeds through
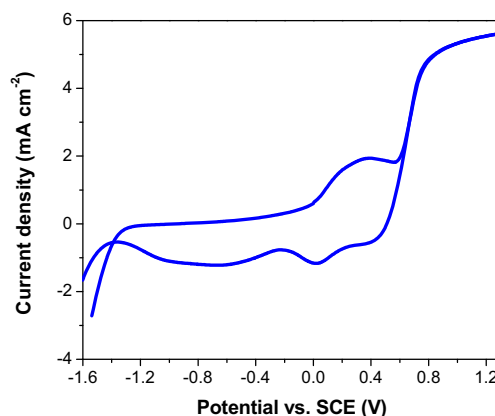

Fig. 7 Ragone plot of Ni-Mo-Ir-oxide electrodes studied in this work

Fig. 8 Cyclic voltammogram of the Ni$_{0.36}$Mo$_{0.24}$Ir$_{0.4}$-oxide electrode recorded in a three-electrode cell in 6-M KOH at a scan rate of 10 mV s^{-1}
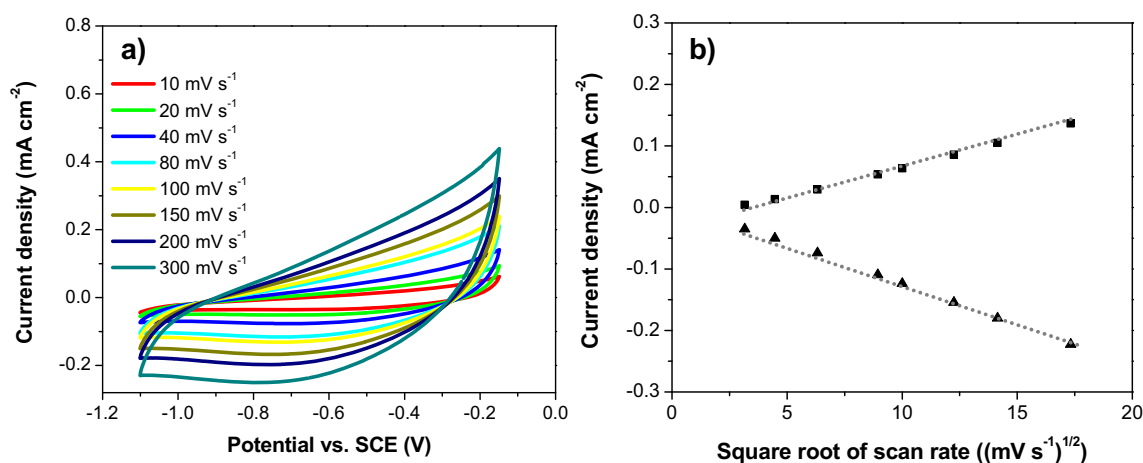
Fig. 9 **a** Cyclic voltammograms of the $Ni_{0.36}Mo_{0.24}Ir_{0.4}$-oxide electrode recorded in the pseudocapacitive region, at different scan rates, in 6-M KOH. **b** Variation of the anodic (black square) and cathodic (black triangle) current recorded at -0.6 V versus the square root of scanning rates

Eq. 1, one can assume that the current response in Fig. 9 is controlled by mass-transport of protons in the oxide phase.

Finally, the performance of the $Ni_{0.36}Mo_{0.24}Ir_{0.4}$-oxide coating was investigated over 2500 charge-discharge cycles. The results are presented in Fig. 10. Overall, Fig. 10 evidences an initial decrease in capacitance, with a total capacitance retention of 86% after 2500 cycles. As it can be seen, during the initial 500 cycles, the capacitance value decreased more sharply from 108 ± 2 to 95 ± 2 mF cm^{-2} and then gradually reached a value of 93 ± 2 mF cm^{-2}. Possible causes for the capacitance decline of the electrodes in the first 500 cycles can be related to the partial dissolution of the $Ni_{0.38}Mo_{0.24}Ir_{0.4}$-oxide coating into the electrolyte, to a decrement of the surface area exposed to the electrolyte, or structural changes within the topmost part of the coating [38]. However, the percentage of retention obtained for this specific electrode is much higher than for some reported in several studies on mixed metal oxide–based electrodes [20, 41].
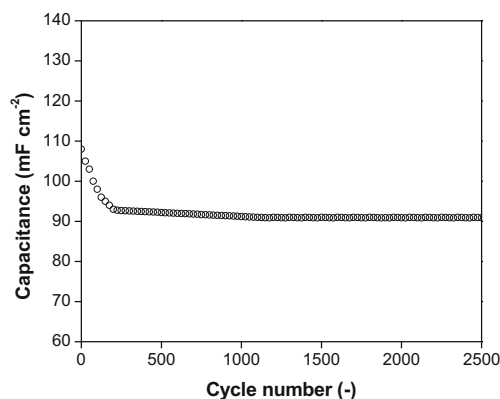
Conclusions

Ni-Mo-Ir-oxide coatings exhibited a high specific capacitance, excellent cycling stability, and a fast charge-discharge rate, which make them promising electrode materials for supercapacitors. The highest capacitance was obtained for the composition that contained 40 mol% of Ir ($Ni_{0.36}Mo_{0.24}Ir_{0.4}$-oxide). The $Ni_{0.36}Mo_{0.24}Ir_{0.4}$-oxide was found to retain ca. 86% of its initial capacitance after 2500 charge-discharge cycles, at 1 mA cm^{-2} in alkaline medium. Based on these findings, the authors' opinion is that the $Ni_{0.36}Mo_{0.24}Ir_{0.4}$-oxide composition is possibly a suitable candidate material for fabrication of supercapacitor electrodes based on the metal oxide nanoparticle/carbon composites.

Fig. 10 Dependence of capacitance of the $Ni_{0.36}Mo_{0.24}Ir_{0.4}$-oxide electrode on the number of charge-discharge cycles recorded in 6-M KOH at 1 mA cm^{-2}

References

1. McArthur M, Hordy N, Coulombe S, Omanovic S (2015) A binder-free multi-walled carbon nanotube electrode containing oxygen functionalities for electrochemical capacitors. Electrochim Acta 162:245–253
2. Simon P, Gogotsi Y (2010) Materials for electrochemical capacitors. In: Nanoscience and technology: a collection of reviews from nature journals. World Scientific, Singapore, pp 320–329
3. Cho M-Y, Kim M-H, Kim H-K, Kim K-B, Yoon JR, Roh KC (2014) Electrochemical performance of hybrid supercapacitor fabricated using multi-structured activated carbon. Electrochem Commun 47:5–8
4. Chen Y-M, Cai J-H, Huang Y-S, Lee K-Y, Tsai D-S, Tiong K-K (2011) A nanostructured electrode of IrOx foil on the carbon nanotubes for supercapacitors. Nanotechnology 22(35):355708

5. Inamdar A, Kim Y, Pawar S, Kim J, Im H, Kim H (2011) Chemically grown, porous, nickel oxide thin-film for electrochemical supercapacitors. J Power Sources 196(4):2393–2397

6. Pang SC, Anderson MA, Chapman TW (2000) Novel electrode materials for thin-film ultracapacitors: comparison of electrochemical properties of sol-gel-derived and electrodeposited manganese dioxide. J Electrochem Soc 147(2):444–450

7. Ganesh V, Lakshminarayanan V, Pitchumani S (2005) Assessment of liquid crystal template deposited porous nickel as a supercapacitor electrode material. Electrochem Solid-State Lett 8(6):A308–A312

8. Mastragostino M, Arbizzani C, Soavi F (2002) Conducting polymers as electrode materials in supercapacitors. Solid State Ionics 148(3-4):493–498

9. Xia X-h, J-p T, Y-j M, X-l W, C-d G, X-b Z (2011) Self-supported hydrothermal synthesized hollow Co3O4 nanowire arrays with high supercapacitor capacitance. J Mater Chem 21(25):9319–9325

10. Shakir I, Nadeem M, Shahid M, Kang DJ (2014) Ultra-thin solution-based coating of molybdenum oxide on multiwall carbon nanotubes for high-performance supercapacitor electrodes. Electrochim Acta 118:138–142

11. Nelson PA, Owen JR (2003) A high-performance supercapacitor/battery hybrid incorporating templated mesoporous electrodes. J Electrochem Soc 150(10):A1313–A1317

12. Nam K-W, Lee E-S, Kim J-H, Lee Y-H, Kim K-B (2005) Synthesis and electrochemical investigations of Ni1− x O thin films and Ni1− x O on three-dimensional carbon substrates for electrochemical capacitors. J Electrochem Soc 152(11):A2123–A2129

13. Nam K-W, Kim K-B (2002) A study of the preparation of NiO x electrode via electrochemical route for supercapacitor applications and their charge storage mechanism. J Electrochem Soc 149(3):A346–A354

14. Xie Y, Huang C, Zhou L, Liu Y, Huang H (2009) Supercapacitor application of nickel oxide–titania nanocomposites. Compos Sci Technol 69(13):2108–2114

15. Shakir I, Shahid M, Cherevko S, Chung C-H, Kang DJ (2011) Ultrahigh-energy and stable supercapacitors based on intertwined porous MoO3–MWCNT nanocomposites. Electrochim Acta 58:76–80

16. Conway BE (2013) Electrochemical supercapacitors: scientific fundamentals and technological applications. Springer Science & Business Media, Berlin

17. Deng L, Wang J, Zhu G, Kang L, Hao Z, Lei Z, Yang Z, Liu Z-H (2014) RuO2/graphene hybrid material for high performance electrochemical capacitor. J Power Sources 248:407–415

18. Poonguzhali R, Shanmugam N, Gobi R, Senthilkumar A, Viruthagiri G, Kannadasan N (2015) Effect of Fe doping on the electrochemical capacitor behavior of MnO2 nanocrystals. J Power Sources 293:790–798

19. Thind SS, Chang X, Wentzell JS, Chen A (2016) High-performance supercapacitor based on tantalum iridium oxides supported on tungsten oxide nanoplatelets. Electrochem Commun 67:1–5

20. Yuan C-Z, Gao B, Zhang X-G (2007) Electrochemical capacitance of NiO/Ru0. 35V0. 65O2 asymmetric electrochemical capacitor. J Power Sources 173(1):606–612

21. Lang X, Hirata A, Fujita T, Chen M (2011) Nanoporous metal/oxide hybrid electrodes for electrochemical supercapacitors. Nat Nanotechnol 6(4):232–236

22. Vidales AG, Omanovic S (2018) Evaluation of nickel-molybdenum-oxides as cathodes for hydrogen evolution by water electrolysis in acidic, alkaline, and neutral media. Electrochim Acta 262:115–123

23. Vidales AG, Choi K, Omanovic S (2018) Nickel-cobalt-oxide cathodes for hydrogen production by water electrolysis in acidic and alkaline media. Int J Hydrog Energy 4:12917–12928

24. Vidales AG, Dam-Quang L, Hong A, Omanovic S (2019) The influence of addition of iridium-oxide to nickel-molybdenum-oxide cathodes on the electrocatalytic activity towards hydrogen evolution in acidic medium and on the cathode deactivation resistance. Electrochim Acta 302:198–206

25. Chang J, Park M, Ham D, Ogale S, Mane RS, Han S-H (2008) Liquid-phase synthesized mesoporous electrochemical supercapacitors of nickel hydroxide. Electrochim Acta 53(15):5016–5021

26. Lei F, Sun Y, Liu K, Gao S, Liang L, Pan B, Xie Y (2014) Oxygen vacancies confined in ultrathin indium oxide porous sheets for promoted visible-light water splitting. J Am Chem Soc 136(19):6826–6829. https://doi.org/10.1021/ja501866r

27. Topalov G, Ganske G, Lefterova E, Schnakenberg U, Slavcheva E (2011) Preparation and properties of thin Pt–Ir films deposited by dc magnetron co-sputtering. Int J Hydrog Energy 36(23):15437–15445. https://doi.org/10.1016/j.ijhydene.2011.08.100

28. Kötz R, Neff H, Stucki S (1984) Anodic iridium oxide films XPS-studies of oxidation state changes and. J Electrochem Soc 131(1):72–77

29. Dupin J-C, Gonbeau D, Vinatier P, Levasseur A (2000) Systematic XPS studies of metal oxides, hydroxides and peroxides. Phys Chem Chem Phys 2(6):1319–1324

30. Li H, Yu M, Wang F, Liu P, Liang Y, Xiao J, Wang C, Tong Y, Yang G (2013) Amorphous nickel hydroxide nanospheres with ultrahigh capacitance and energy density as electrochemical pseudocapacitor materials. Nat Commun 4:1894

31. Kulal P, Dubal D, Lokhande C, Fulari V (2011) Chemical synthesis of Fe2O3 thin films for supercapacitor application. J Alloys Compd 509(5):2567–2571

32. Chen Y, Wang Y, Sun P, Yang P, Du L, Mai W (2015) Nickel oxide nanoflake-based bifunctional glass electrodes with superior cyclic stability for energy storage and electrochromic applications. J Mater Chem A 3(41):20614–20618

33. Kötz R, Carlen M (2000) Principles and applications of electrochemical capacitors. Electrochim Acta 45(15-16):2483–2498

34. Conway B, Birss V, Wojtowicz J (1997) The role and utilization of pseudocapacitance for energy storage by supercapacitors. J Power Sources 66(1-2):1–14

35. Chuang C-M, Huang C-W, Teng H, Ting J-M (2010) Effects of carbon nanotube grafting on the performance of electric double layer capacitors. Energy Fuel 24(12):6476–6482

36. Chuang C-M, Huang C-W, Teng H, Ting J-M (2012) Hydrothermally synthesized RuO2/carbon nanofibers composites for use in high-rate supercapacitor electrodes. Compos Sci Technol 72(13):1524–1529

37. Frackowiak E, Beguin F (2001) Carbon materials for the electrochemical storage of energy in capacitors. Carbon 39(6):937–950

38. Jiang F, Li W, Zou R, Liu Q, Xu K, An L, Hu J (2014) MoO3/PANI coaxial heterostructure nanobelts by in situ polymerization for high performance supercapacitors. Nano Energy 7:72–79

39. Ullah N, McArthur MA, Omanovic S (2015) Iridium-ruthenium-oxide coatings for supercapacitors. Can J Chem Eng 93(11):1941–1948

40. Raj CJ, Rajesh M, Manikandan R, Sim JY, Yu KH, Park SY, Song JH, Kim BC (2017) Two-dimensional planar supercapacitor based on zinc oxide/manganese oxide core/shell nano-architecture. Electrochim Acta 247:949–957

41. McArthur MA, Ullah N, Coulombe S, Omanovic S (2018) A binder-free Ir0. 4Ru0. 6-oxide/functionalized multi-walled carbon nanotube electrode for possible applications in supercapacitors. Can J Chem Eng 96(1):74–82

42. Rakhi R, Chen W, Cha D, Alshareef HN (2012) Substrate dependent self-organization of mesoporous cobalt oxide nanowires with remarkable pseudocapacitance. Nano Lett 12(5):2559–2567

43. Aytaç A, Gürbüz M, Sanli AE (2011) Electrooxidation of hydrogen peroxide and sodium borohydride on Ni deposited carbon fiber electrode for alkaline fuel cells. Int J Hydrog Energy 36(16): 10013–10021

44. Saji VS, Lee CW (2012) Molybdenum, molybdenum oxides, and their electrochemistry. ChemSusChem 5(7):1146–1161

45. Pourbaix M, Van Muylder J, De Zoubov N (1959) Electrochemical properties of the platinum metals. Platin Met Rev 3:47–53

46. Pletcher D, Greff R, Peat R, Peter L, Robinson J (2001) Instrumental methods in electrochemistry. Elsevier, Amsterdam